Strain localization and ductile fracture in advanced high-strength steel sheets

G. Gruben[1,2,3], D. Morin[1,2*], M. Langseth[1,2] and O.S. Hopperstad[1,2]

[1]Centre for Advanced Structural Analysis, Centre for Research-based Innovation (CRI), NTNU, Norwegian University of Science and Technology, NO-7491 Trondheim, Norway

[2]Department of Structural Engineering, NTNU, Norwegian University of Science and Technology, NO-7491 Trondheim, Norway

[3]SINTEF Materials and Chemistry, Rich. Birkelands vei 2B, NO-7491 Trondheim, Norway

Abstract

An experimental-numerical approach is applied to determine the strain localization and ductile fracture of high-strength dual-phase and martensitic steel sheet materials. To this end, four different quasi-static material tests were performed for each material, introducing stress states ranging from simple shear to equi-biaxial tension. The tests were analysed numerically with the nonlinear finite element method to estimate the failure strain as a function of stress state. The effect of spatial discretization on the estimated failure strain was investigated. While the global response is hardly affected by the spatial discretization, the effect on the failure strain is large for tests experiencing necking instability. The result is that the estimated failure strain in the different tests scales differently with spatial discretization. Localization analysis was performed using the imperfection band approach, and applied to estimate onset of failure of the two steel sheet materials under tensile loading. The results indicate that a conservative failure criterion for ductile materials may be established from localization analysis, provided strain localization occurs prior to ductile fracture.

Keywords: Ductile fracture; Stress triaxiality; Lode parameter; Finite element method, Strain localization

1 Introduction

The physical mechanism leading to ductile fracture in polycrystalline materials is nucleation and growth of microvoids [1, 2]. When the microvoids reach a certain volume fraction, they

* Corresponding author. Tel.: + 47 46542691

E-mail address: david.morin@ntnu.no (D. Morin).

induce plastic flow localization before the material is torn apart. Tekoğlu et al. [3] investigated the competition between plastic flow localization occurring either as shear banding due to material softening or as internal necking and void coalescence in the ligament between the microvoids. Onset of strain localization due to either of the two aforementioned mechanisms is influenced by the stress state. A commonly used parameter to describe the hydrostatic stress state is the stress triaxiality, σ^*, which is the ratio of the hydrostatic stress and the von Mises equivalent stress. Increased stress triaxiality increases the rate of void growth and so decreases the material's ductility, e.g. [4-7]. Recent findings from macro-scale experiments [8-11] and unit cell models [12-14] show that the deviatoric stress state also influences the ductility at low levels of stress triaxiality. The deviatoric stress state can be described by the Lode parameter, μ [15], which expresses the position of the second principal stress in relation to the major and minor principal stresses. For thin sheets in plane stress conditions, the stress triaxiality is bounded, $-2/3 \le \sigma^* \le 2/3$, and there is a relation between σ^* and μ [16]. Since structural components intended to absorb energy in accidental loading conditions for instance in cars and ships often are built up by sheets or plates, failure under plane-stress conditions is important and the influence of the plane stress state on the material's ductility should be well understood for enhancement of future design.

The most commonly used macroscopic measure to describe ductility is the equivalent plastic strain at onset of plastic flow localization or material failure, p_f. For strain fields with high gradients, strain values depend strongly on the size of the region over which they are derived. In the late 19th century, Barba [17] encountered this phenomenon in uniaxial tensile tests experiencing diffuse necking and estimated the engineering failure strain by dividing the elongation into a uniform part which is independent of the gauge length and a non-uniform part which depends on the gauge length and needs to be calibrated for a specific material. According to Barba's law, the engineering failure strain, e_f, in a uniaxial tension test is expressed as [17]

$$e_f = \beta \frac{\sqrt{A_0}}{L_0} + e_u \tag{1}$$

where A_0 is the initial cross section area, L_0 is the initial gauge length, e_u is the uniform engineering strain and β is a calibration constant. Modified versions of Barba's law where the equivalent plastic strain at failure, p_f, is taken as a function of the element size have been applied in numerical simulations involving ductile fracture in large structures [18-20].

Traditionally the ductility of a material at various stress states is established through an experimental-numerical approach where the strain and stress histories from the critical location in the test specimen are found from Finite Element (FE) simulations, e.g. [7, 8, 21-26]. Optical measurements, using for instance Digital Image Correlation (DIC), could be applied for this purpose, but DIC measurements are limited to provide information about the kinematic fields on the surface of the specimen. On the contrary, FE simulations provide kinematic as well as kinetic fields in all parts of the specimen. FE models also have more flexibility regarding spatial discretization compared to DIC measurements, but depend on an appropriate and well-calibrated constitutive model. In general, smaller DIC elements are more prone to image noise than larger elements, while larger DIC elements are less capable of describing displacement fields with high gradients [27]. In FE simulations the lower limit of the element size is only governed by practical aspects concerning the computational time, while the upper limit follows the same restrictions as in the DIC analysis. As pointed out previously, e.g. [10, 28], a converged solution of the global response curves (e.g. the force-displacement curve) does not imply a converged solution of the local deformation in the region of plastic flow localization.

Ductile failure in metals is the final stage of a series of complex phenomena and is often preceded by strain localization in form of a shear band. By assuming that failure occurs shortly after the onset of localization, it is therefore possible to evaluate the ductility of a material by using a criterion for strain localization. Several criteria of this type have been proposed in the literature, some of them tailored to plane-stress states, such as the Marciniak-Kuczynski approach [29], while others, such as the imperfection analysis proposed by Rice [30] and later used in several other studies, e.g. [31-35], allows for analysis of 3D stress states.

In the present study, the failure strain as a function of stress state is determined for two types of advanced high-strength steel sheet materials using an experimental-numerical approach comprising four different material tests. The effect of spatial discretization in the FE simulations on the estimated failure strain is investigated by increasing the polynomial order of the elements positioned in the most severely deformed regions. This means that the failure strain and stress state are averaged over the same material volume in all cases, but the interpolation of the displacements inside this volume varies. Localization analyses are applied to estimate failure under tensile loading and the results are compared with the failure strains obtained by means of the experimental-numerical approach.

2 Experimental programme

In this study, the stress-strain behaviour and ductile failure of dual-phase Docol 600DL and martensitic Docol 1400M steel sheet materials were investigated. The Docol 600 DL sheet had 1.8 mm thickness, while the thickness of the Docol 1400M sheet was 1.0 mm. Docol 600DL is a low-strength, high-hardening material, where the ferrite gives good formability and the martensite provides increased strength. Docol 1400M is a high-strength steel where very fast water quenching from the austenitic temperature range produces the high strength. Uniaxial tensile tests carried out on tensile specimens cut out at 0°, 45° and 90° to the rolling direction were presented in [36]. Both materials were found to be nearly isotropic.

All tests were carried out at room temperature under quasi-static loading conditions. The uniaxial tension and in-plane simple shear tests were presented in [36] and used to calibrate constitutive models. These tests are described here with more emphasis on ductility. The four selected tests provide a wide range of stress states before onset of fracture. Some of these tests exhibit nearly proportional loading and others non-proportional loading due to diffuse and/or local necking.

2.1 Optical measurements

All the tests were recorded by digital cameras. One camera was used for 2D measurements and two cameras for 3D measurements of the displacement field on the surface of the specimens. The cameras were of the type Prosilica GC2450 equipped with 50 mm Nikon lenses. Before testing a combination of black and white paint was spray-painted on the side of the specimen facing the camera(s), thus obtaining a high-contrast speckle pattern which improved the optical measurements. The displacement fields and the associated strain fields on the surface of the specimen were extracted from the images by applying an in-house finite element based DIC software which employs initially square bilinear Q4 elements [27]. As an experimental measure of the material’s ductility in the different tests, the strain magnitude field was calculated. The strain magnitude (or effective strain) at a given point is here defined as

$$\varepsilon_e = \sqrt{\frac{2}{3}\left(\varepsilon_1^2 + \varepsilon_2^2 + \varepsilon_3^2\right)} \tag{2}$$

where $\varepsilon_i = \ln(\lambda_i)$, $i = 1,2$, are the logarithmic in-plane principal strains, where λ_i^2 are the eigenvalues of the right Cauchy-Green deformation tensor. The through-thickness principal strain is estimated as $\varepsilon_3 = -(\varepsilon_1 + \varepsilon_2)$ based on plastic incompressibility and by neglecting elastic deformations.

2.2 Uniaxial tension tests

The nominal geometry of the uniaxial tension (UT) test specimen is given in Fig. 1(a). Three parallel tests were carried out under displacement control in a hydraulic Zwick/Roell tensile testing machine with a capacity of 30 kN. The loading rate was 4 mm/min, thus providing a strain rate before necking of $1.0 \cdot 10^{-3}\ \text{s}^{-1}$. The tests were performed with tension along the rolling direction of the sheet. The force was measured by a load cell in the hydraulic actuator, while displacements were collected by a virtual extensometer based on DIC with initial length $L_0 = 60\ \text{mm}$, see Fig. 2(a). The engineering stress, s, and engineering strain, e, were calculated as $s = F / A_0$ and $e = (L - L_0) / L_0$, where F is the force measured by the load cell, A_0 is the measured initial cross-section area of the specimen, and L is the extensometer gauge length. Fig. 3(a) and (e) show the engineering stress-strain curves for Docol 600DL and Docol 1400M, respectively.

The tests were recorded at a frequency of 2 images per second, and the strains were calculated from the displacement field using an initial nodal spacing of 1.2 mm. The strain magnitude field in the last image before fracture, ε_e^f, of one of the duplicates is shown in Fig. 4(a) and (e) for Docol 600DL and Docol 1400M, respectively. As can be seen, the main deformation mode before fracture is diffuse necking in the test on Docol 600DL, while the specimen made of Docol 1400M fractures along a local neck. The maximum strain magnitude is ~0.7 for Docol 600DL and ~0.4 for Docol 1400M.

2.3 Plane-strain tension tests

The plane-strain tension (PST) tests were conducted in an Instron 5900 hydraulic tensile testing machine. The hydraulic actuator had a loading rate of 0.9 mm/min which gave an initial strain rate in the gauge area of $1.0 \cdot 10^{-3}\ \text{s}^{-1}$. The nominal geometry of the PST specimen is illustrated in Fig. 1(b). The specimens were cut out with the longitudinal axis in the rolling direction of the sheet. A virtual extensometer with an initial length of 18.5 mm was applied to collect the displacements, see Fig. 2(b), while the force was measured by the load cell of the hydraulic testing machine, using a synchronized logging with frequency 2 Hz. To account for variations in the initial cross-section, a normalized force was calculated as F / A_0, where F is the measured force in the load cell and A_0 is the measured initial cross-section of the specimen.

The normalized force versus displacement curves from the three parallel tests of the two materials are given in Fig. 3(b) and (f). Two of the tests on the 1400M material displayed larger displacement at failure than the third. From the camera recordings, it was observed that this was due to a minor misalignment in the two tests, which again led to a slightly different stress-state during deformation and larger ductility. Fig. 4(b) and (f) display the strain magnitude field in the last image before onset of fracture in a selected test for Docol 600DL and the test without misalignment for Docol 1400M. The initial distance between the nodes in the DIC meshes was 1.0 mm. The resulting strain magnitude before fracture was ~0.5 and ~0.2 for the dual-phase and martensitic steels, respectively.

2.4 In-plane simple shear tests

The in-plane simple shear (ISS) tests were conducted under displacement control in the same Zwick/Roell tensile test machine used for the UT tests. The applied loading rate was 0.3 mm/min which gave an initial strain rate of $1.0 \cdot 10^{-3}$ s^{-1}. The specimens were cut so that the longitudinal axis corresponds to the rolling direction of the sheet. Fig. 1(c) presents the geometry of the ISS specimen. A virtual extensometer measured the displacement near the gauge area, see Fig. 2(c), while the force was measured by the load cell in the hydraulic testing machine. The normalized force versus displacement curves from the three parallel tests are given in Fig. 3(c) and (g), where the normalized force F / A_0 is the ratio between the measured force F and the initial gauge area A_0 of the shear test specimen.

The camera was recording the tests at a framing rate of 1 Hz, and the initial nodal spacing in the DIC grid was 0.5 mm. The strain magnitude field in the last image before onset of fracture was ~1.0 for Docol 600DL and ~0.60 for Docol 1400M, as shown in Fig. 4(c) and (g). Evidently the gauge zone has rotated before failure and the strain localizes in a thin band inclined with respect to the loading direction.

2.5 Nakajima tests

The Nakajima test set-up [37] was applied with specimens designed to obtain equi-biaxial tension. Four parallel Nakajima (NK) tests were carried out in a Zwick/Roell BUP 600 test machine under displacement control with a punch velocity of 0.3 mm/s. The specimen geometry is presented in Fig. 1(d), while Fig. 1(e) shows the specimen clamped between the die and the blank holder and loaded by the punch. The clamping force can be altered, and the appropriate value may vary for different materials and sheet thicknesses. In this study, the clamping force was set to 360 kN in the tests on Docol 600DL and 200 kN in the test on Docol 1400M. To ensure failure close to the centre of the specimen, the punch was lubricated with grease before a 0.1 mm thick layer of Teflon was placed between the punch and the specimen. The force and displacement of the punch were recorded by the testing machine. Fig. 3(d) and (h) give the force-displacement curves obtained from the tests.

To capture the out-of-plane deformation, two cameras were used to record images of the experiments at a framing rate of 2 Hz. A grid with an initial nodal spacing of 1.3 mm was applied in recording the displacement fields and deriving the strain fields on the surface of the specimen. As shown in Fig. 4(d) and (h), the strain magnitude is ~1.0 for the dual-phase steel and ~0.50 for the martensitic steel just before fracture.

3 Modelling and simulation

Modelling and simulation of the experimental tests were carried out with the nonlinear explicit finite element programme IMPETUS AFEA [38].

3.1 Constitutive model

Constitutive models of the steel sheet materials were calibrated in [36], adopting the high-exponent Hershey yield function [39] with associated plastic flow and isotropic hardening. The dynamic yield function is given by

$$f = \varphi(\boldsymbol{\sigma}) - \sigma_f(p, \dot{p}) = 0 \tag{3}$$

$$\sigma_{eq} \equiv \varphi(\boldsymbol{\sigma}) = \left(\tfrac{1}{2}\left((\sigma_I - \sigma_{II})^m + (\sigma_{II} - \sigma_{III})^m + (\sigma_I - \sigma_{III})^m\right)\right)^{\frac{1}{m}} \tag{4}$$

$$\sigma_f(p, \dot{p}) = \left(\sigma_0 + \sum_{i=1}^{3} Q_i\left(1 - \exp(-C_i p)\right)\right) \cdot \left(1 + \frac{\dot{p}}{\dot{p}_0}\right)^c \tag{5}$$

where $\sigma_I \geq \sigma_{II} \geq \sigma_{III}$ are the ordered principal stresses, m is an exponent controlling the shape of the yield surface, $\dot{p}$ is the equivalent plastic strain-rate which is power conjugate with the equivalent stress, $\sigma_{eq} \equiv \varphi(\boldsymbol{\sigma})$, and $p = \int \dot{p}dt$ is the equivalent plastic strain. Further, σ_f is the flow stress, σ_0 is the initial yield stress, Q_i and C_i $(i = 1,2,3)$ are parameters governing the work hardening, whereas c and $\dot{p}_0$ are parameters controlling the rate sensitivity. The identified model parameters are given in Table 1. In order to eliminate the need of a geometrical trigger in the FE model to capture the correct position of the diffuse neck in the simulations of the uniaxial tension tests, the reference strain rates, $\dot{p}_0$, in Table 1 are somewhat larger than those reported in [36].

3.2 Finite element models

Solid elements were used to discretize the test specimens in the finite element (FE) models. Fig. 5 shows the meshes of the four specimens. The FE models utilized symmetry planes in order to reduce the computational time. All applied symmetry planes are indicated in Fig. 5, except for the ones in the through-thickness direction utilized in the UT, PST and ISS models. The UT, PST and NK models were given a refined mesh in the region subjected to the largest deformations, see Fig. 5(a), (b) and (e). In all models, the region subjected to the largest deformation was discretized by hexahedral elements with an in-plane size of 0.25 mm and 6 elements in the thickness direction, i.e., an initial element height of 0.30 mm for the dual-phase sheet and 0.17 mm for the martensitic sheet. In order to investigate the effect of spatial discretization on the ductility assessments while retaining the same gauge volume, simulations were run with elements possessing linear, quadratic and cubic shape functions in the fine-mesh regions. By applying p-refinement, the element configuration was the same in the three runs of each test. All three element types follow a Gauss-Legendre quadrature. The linear elements have selectively reduced integration, while the quadratic and cubic elements are fully integrated. The linear element has $2^3 = 8$ nodes, the quadratic element has $3^3 = 27$ nodes and the cubic element has $4^3 = 64$ nodes.

Since IMPETUS AFEA follows an explicit time integration scheme, uniform mass scaling was applied to increase the critical time step in the simulations. The amount of mass scaling was independent of polynomial order, and the initial stable time step in the simulations of the martensitic steel sheet, Δt_{cr}, was $5.0 \cdot 10^{-4}$, $4.0 \cdot 10^{-4}$ and $3.5 \cdot 10^{-4}$ s for elements with linear, quadratic and cubic shape functions respectively, while Δt_{cr} in the simulations of the dual-phase steel sheet was approximately two times larger than these values. It was checked in all simulations that the kinetic energy was negligible compared with the internal energy, thus ensuring a quasi-static loading process.

In the simulations of the uniaxial tension and plane-strain tension tests, the loading was a prescribed velocity applied to rigid body (RB) parts positioned an appropriate distance from the gauge region, see Fig. 5(a) and (b). The prescribed velocity was ramped up over the first 15 s of the simulation using a smooth transition function. In the simulations of the in-plane simple shear test, prescribed displacements collected from DIC measurements obtained in one experimental duplicate were applied as local boundary conditions on nodes close to the gauge region. Here the same in-plane loading was applied through the thickness of the FE model. This method ensured correct rotation of the gauge region. In the simulations of the Nakajima tests, a Coulomb friction model with a tangential friction coefficient of 0.01 was applied in the punch-specimen interface. The draw-bead was not included in the model as it was found that constraining the outermost nodes of the specimen from in-plane movement and specifying a tangential friction coefficient of 0.4 for the specimen-blank holder and specimen-die interfaces gave appropriate boundary conditions. The upper part of the die and the lower part of the blank holder were constrained to avoid translational displacement. Loading was applied by ramping up the punch velocity to 0.3 mm/s over the first 15 s by use of a smooth transition function.

3.3 Localization analysis

We consider a homogeneously deformed body in which a thin planar band with a small imperfection is present. The stress and strain rates as well as the constitutive relations inside this band are allowed to be different from those outside the band, but equilibrium across the band is enforced. The equations for continuing equilibrium are expressed as [30]

$$\mathbf{n}_0 \cdot \dot{\mathbf{P}}_b = \mathbf{n}_0 \cdot \dot{\mathbf{P}} \tag{6}$$

where $\mathbf{n}_0$ is the normal to the band expressed in the reference configuration and $\dot{\mathbf{P}}$ is the rate of the nominal stress tensor. The subscript b denotes a quantity inside the band. Compatibility implies that the velocity field can only vary along the normal direction of the planar band and thus

$$\mathbf{L}_b = \mathbf{L} + \dot{\mathbf{q}} \otimes \mathbf{n} \tag{7}$$

where $\mathbf{L}_b$ and $\mathbf{L}$ are the velocity gradient tensors respectively inside and outside the band, $\mathbf{n}$ is the normal of the band in the current configuration, and $\dot{\mathbf{q}}$ is a vector that represents the rate of the deformation non-uniformity. Assuming rate-independent plasticity and adopting an updated Lagrangian formulation, where the reference configuration is taken to coincide momentarily with the current configuration, the rate constitutive equations may be expressed in the form

$$\dot{\mathbf{P}} = \mathbf{C}^t : \mathbf{L} \quad \text{and} \quad \dot{\mathbf{P}}_b = \mathbf{C}_b^t : \mathbf{L}_b \tag{8}$$

where $\mathbf{C}^t$ and $\mathbf{C}_b^t$ are the continuum tangent operators outside and inside the band, respectively (see [30-32] for details).

Loss of ellipticity, or strain localization, occurs when the acoustic tensor $\mathbf{A}^t(\mathbf{n}) \equiv \mathbf{n} \cdot \mathbf{C}_b^t \cdot \mathbf{n}$ becomes singular [30], viz.

$$\det\left(\mathbf{n} \cdot \mathbf{C}_b^t \cdot \mathbf{n}\right) = 0 \tag{9}$$

For material undergoing associated plastic flow, this condition is not met unless strain softening is present in the constitutive response of the material or in the imperfection band for this particular case. Strain softening in ductile metals is often linked to damage evolution and/or thermal softening. In this study, the Gurson model [40] for porous plasticity is adopted to model the material behaviour inside the band, thus to describe strain softening due to void growth and eventually loss of ellipticity inside the band. The Gurson model is an appealing approach to include strain softening into a constitutive model due to its limited number of parameters.

The yield function of the Gurson model is defined as [40, 41]

$$f = \frac{\varphi^2(\boldsymbol{\sigma})}{\sigma_M^2} + 2q_1\omega\cosh\left(\frac{3}{2}q_2\frac{\boldsymbol{\sigma}:\mathbf{I}}{\sigma_M}\right) - \left(1 + q_3\omega^2\right) = 0 \tag{10}$$

where $\sigma_{eq} \equiv \varphi(\boldsymbol{\sigma})$ is the equivalent stress, σ_M is the flow stress of the matrix, ω is the porosity and $\mathbf{I}$ is the second-order identity tensor. The material parameters of the Gurson model are taken from Tvergaard [41]: $q_1 = 1.5$, $q_2 = 1.0$ and $q_3 = 2.25$. The work hardening of the matrix material is described by Eq. (5), using the parameters in Table 1, but the rate-sensitivity is neglected in the localization analysis. This will result in more conservative results for the strain at localization. Since the Hershey yield function is adopted for the steel sheet materials, a heuristic modification of the Gurson model is implemented. The von Mises equivalent stress used in the original Gurson model is replaced with the Hershey equivalent stress as defined by Eq. (4). Steglich et al. [42] employed a similar type of heuristic modification of the Gurson model using the high-exponent Bron-Besson yield function for anisotropic materials.

When using the Gurson model to describe strain softening, the porosity ω requires an initial value ω_0 as well as an evolution rule. In the literature, the void evolution rule is usually decomposed as follows

$$\dot{\omega} = \dot{\omega}_g + \dot{\omega}_n + \dot{\omega}_s \tag{11}$$

where $\dot{\omega}_g$ is the void growth linked to the volumetric plastic strain rate, as obtained from the associated flow rule, $\dot{\omega}_n$ is related to the nucleation of voids, and $\dot{\omega}_s$ corresponds to the shearing of voids. While the growth and nucleation of voids are well-established phenomena [43], the shearing of voids has been proposed quite recently [34] and is still under discussion [44, 45]. Shearing of voids is assumed to be an important feature to describe ductile failure under low stress triaxiality (typically close to pure shear). Several studies in the literature have applied the Gurson model to dual-phase steels [46, 47] and the initial void content ω_0 is usually small (between 0 and 1×10^{-5}). Void nucleation in dual-phase steels can be linked to debonding between the ferrite and martensite [48]. To limit the complexity of the strain-softening model of this study, it was chosen to exclude void nucleation and void shearing—and thus only to include void growth. The implication is that failure under low triaxiality cannot be predicted. The initial porosity ω_0 is considered here as an initial imperfection. Hence, the physical relevance of ω becomes less clear. To some extent, this simplification can be related to the initial imperfection of the Marciniak-Kuczynski analysis [29].

The localization analyses are carried out using the velocity gradient $\mathbf{L}$ extracted from the finite element simulations in the elements where failure is assumed to occur. Based on these data, the stress state outside the band was re-computed assuming rate-independent plasticity by a stand-alone FORTRAN code. The same solver was used to enforce equilibrium for the imperfection band, to determine its local stress state and to estimate loss of ellipticity. Due to the numerical aspects of the localization analysis, loss of ellipticity is assumed to occur when the determinant of the acoustic tensor becomes negative. A schematic illustration of the procedure is given in Fig. 6. The band orientation in the reference configuration is given by its unit normal vector

$$\mathbf{n}_0 = \begin{Bmatrix} \cos\phi_0 \\ \cos\theta_0 \sin\phi_0 \\ \sin\theta_0 \sin\phi_0 \end{Bmatrix} \tag{12}$$

where $\phi_0 \in \left[0, \frac{\pi}{2}\right]$ and $\theta_0 \in \left[0, 2\pi\right]$ are the polar and azimuthal angles of a spherical coordinate system with X_1, X_2, X_3 axes aligned with the rolling direction (RD), in-plane transverse direction (TD) and normal direction (ND) of the sheet material, respectively. To find the minimum ductility, several bands are spread in the (ϕ_0, θ_0) space and the one producing the lowest strain at localization is chosen as the critical one. This operation is repeated iteratively, narrowing down the range of angles at each iteration. This leads to a sub-degree accuracy on the orientation of the critical band and a converged localization strain to within $\pm 1\times 10^{-4}$.

By extracting the velocity gradient $\mathbf{L}$ from the numerical simulations at 1000 equi-distant points of time instead of each time step, the size of the strain increments in the localization analysis varied. To limit the effect of this time discretisation, a sub-stepping scheme was used in which the norm of the strain increment in the sub-steps was set to 1×10^{-5} and thus good accuracy of the stress update algorithm and the localization analysis was ensured [49].

4 Results and discussion

The experimental-numerical approach adopted in the present study follows a much used methodology, e.g. [8, 22], where the global response curve from the test is compared with the corresponding response curve in the simulation to establish the time at onset of fracture in the simulation, t_f. Fig. 3 shows the global response curves from the experiments up to fracture together with the corresponding results from the numerical simulations. For each of the tests, the response curves in the simulations with the three element types are plotted up to the same time instant defined by t_f. This time instant was chosen to minimize the difference between the average experimental and numerical force and displacement at failure. Note that for the PST simulation of the 1400M material, t_f is defined from the test assumed to be closest to a plane-strain tension stress-state. The inserts show the final part of the response curves from simulations and experiments. As can be seen, the strains (or the displacements) at t_f in the simulations with different element types are very similar for all tests, which was expected since loading was applied under displacement control. On the other hand, the difference in the stresses (or the forces) between the linear and cubic element simulations is ~5% for the UT simulations and the PST simulation for Docol 1400M, while the PST simulation for Docol 600DL and the ISS simulations display a difference of ~2%. The simulated global response of the NK tests is independent of the discretization. This shows that the global response curves converge more rapidly in the ISS and NK simulations than in the UT and PST simulations, which are dominated by diffuse and/or local necking before onset of fracture. However, all the linear element simulations may be considered to give a solution that is close to convergence in terms of the global response.

For each simulation, the element in the FE model with the position corresponding to the location of fracture initiation in the experiment was identified. The positions of the critical element are marked by arrows in Fig. 7. Only the in-plane location of fracture initiation was determined from the experiments. In the FE models, the element in the through-thickness direction experiencing the largest equivalent plastic strain was chosen as the critical element. In the UT and PST simulations, this element was located in the centre of the specimen, while in the ISS and NK simulations it was located on the surface of the specimen, although the through-thickness gradient in the equivalent plastic strain was small in the ISS and NK specimens, see Fig. 7.

The evolutions of the stress tensor and the equivalent plastic strain with time were collected from each integration point in the critical element. From the collected history of the stress tensor, the histories of the stress triaxiality, $\sigma_i^*(t)$, and the Lode parameter, $\mu_i(t)$, were calculated for each integration point as

$$\sigma_i^*(t) = \frac{\sigma_{I,i}(t) + \sigma_{II,i}(t) + \sigma_{III,i}(t)}{3\sigma_{VM,i}(t)} \tag{13}$$

$$\mu_i(t) = \frac{2\sigma_{II,i}(t) - \sigma_{I,i}(t) - \sigma_{III,i}(t)}{\sigma_{I,i}(t) - \sigma_{III,i}(t)} \tag{14}$$

where σ_{VM} is the von Mises equivalent stress. In Eqs. (13) and (14), the subscript i denotes the integration point number. For the linear elements the total number of integration points is $n_{ip} = 8$, while for the quadratic and cubic elements n_{ip} equals 27 and 64, respectively. In order to evaluate the effect of p-refinement on the material volume represented by the critical elements, the average values of the equivalent plastic strain, $p(t)$, stress triaxiality $\sigma^*(t)$ and Lode parameter $\mu(t)$ for each critical element were calculated as

$$p(t) = \frac{1}{V}\sum_{i=1}^{n_{ip}} V_i p_i(t), \quad \mu(t) = \frac{1}{V}\sum_{i=1}^{n_{ip}} V_i \mu_i(t), \quad \sigma^*(t) = \frac{1}{V}\sum_{i=1}^{n_{ip}} V_i \sigma_i^*(t) \tag{15}$$

where $V = \Sigma_{i=1}^{n_{ip}} V_i$ is the element volume and V_i is the volume represented by integration point i. It is noted that p-refinement leads to higher DOF density, which is equivalent to refining the spatial discretization. Thus the effect of p-refinement is in the following referred to as the effect of spatial discretization.

Fig. 8 shows the equivalent plastic strain as a function of stress triaxiality and Lode parameter up to onset of fracture, defined by $p(t_f) = p_f$. Table 2 compiles the failure strains p_f together with the average values of the stress triaxiality, σ^*_{avg}, and the Lode parameter, μ_{avg}, which are defined as

$$\sigma^*_{avg} = \frac{1}{p_f}\int_0^{p_f} \sigma^* dp, \qquad \mu_{avg} = \frac{1}{p_f}\int_0^{p_f} \mu dp \tag{16}$$

The average values of stress triaxiality and Lode parameter are plotted in Fig. 9 together with the plane stress locus to illustrate how the tests are distributed in stress space. It is noted that the different element types lead to somewhat different values of the average stress state parameters. As shown in Fig. 8 and Table 2, the dual-phase steel displays a more ductile behaviour than the martensitic steel, which is coherent with the experimental results presented in Fig. 4. Further Fig. 8 shows that the simulations of the NK tests display a more proportional load history than the simulations of the other tests. The simulations of the ISS tests of the dual-phase steel start in compression and moves into tension, while for the martensitic steel the ISS simulations are in tension during the whole simulation. The discrepancy in stress-state history between the ISS simulations of the two materials is mainly related to the difference in the positions of the critical elements, see Fig. 7(c) and (g). It is noted that the quadratic and cubic elements are more prone to volumetric locking than the linear element which applies reduced integration. The kink in the p-σ^* curve and the relatively low p_f value for the UT simulation with cubic elements seen in Fig. 8 (b) may stem from volumetric locking effects.

For both materials, the ISS simulations only display a small variation in p_f for the different element types, while in the NK simulations the variation in p_f with spatial discretization is negligible. The largest dependence on spatial discretization is found in the UT and PST simulations, where the specimens experience necking instability. In these instances, the ratio between the failure strains obtained in simulations with cubic and linear elements is ~1.25 and ~1.5 for the dual-phase and martensitic steels, respectively. Clearly a positive correlation is present between the convergence rates of the global response curves and the local strain values. Note that the failure strain in the linear, quadratic and cubic element simulations is based on the average failure strain within the element following Eq. (15), and that a larger difference is present between the maximum failure strains found within the elements with different p-order.

Fig. 7 shows contour plots of the equivalent plastic strain before estimated onset of fracture in the simulations with cubic elements. The strains are more localized in the martensitic steel than in the dual-phase steel, which was also seen experimentally, cf. Fig. 4. As can be observed from Fig. 7(a) and (e), the UT specimens display high gradients in the strain fields along the thickness, width and longitudinal directions around the critical element, while Fig. 7(b) and (f) show that the PST specimens display high strain gradients in the thickness and longitudinal directions in the vicinity of the critical element. For the ISS specimens in Fig. 7(c) and (g), the critical element experiences high strain gradients only in the in-plane transverse direction, while the critical element in the NK specimens is not subjected to high gradients in the strain fields, as shown in Fig. 7(d) and (h). The equivalent plastic strain in the critical elements of the ISS specimens is not sensitive to spatial discretization despite having high strain gradients along one axis, thus the mesh dependence of the failure strain p_f seems to be linked to the necking instability observed in the UT and PST tests or the presence of high multi-axial strain gradients. This implies that scaling a failure strain based on spatial discretization or gauge length alone, as in some versions of Barba's law, does not necessarily lead to accurate fracture initiation predictions, since material points exposed to necking instability are more sensitive to length scale effects.

The localization analysis was carried out by post-processing results from the FE simulations with cubic elements, as these are assumed to provide the most accurate results. As seen in Fig. 8(b), the simulation of the uniaxial tension tests of the Docol 1400M exhibits some kind of volumetric locking towards the end of the deformation process. The effect of this volumetric locking was a drop in the stress triaxiality which may affect the strain localization. This was checked by carrying out localization analysis based on the data extracted from the simulation of the uniaxial tensile test for Docol 1400M with quadratic elements. No large differences were observed, and therefore, all the results presented below are based on simulations with cubic elements. The failure strains, or localization strains, given below are defined as the equivalent plastic strains computed outside the band at loss of ellipticity. Since neither void nucleation nor void shearing was included in the Gurson model used for the material in the imperfection band, it was not possible to conduct the localization analysis for the in-plane simple shear tests due to the low stress triaxiality.

A parametric study was carried out to find an appropriate size of the initial imperfection ω_0, which gives the best overall agreement with the experimental results. It was tentatively assumed in these simulations that material failure in the experiments was caused by strain localization. For Docol 600DL an initial imperfection of 0.0027 was found, while for Docol 1400M ω_0 was estimated to 0.002. Note that the initial imperfection was identified using the results of finite element simulation and is most-likely mesh dependent.

The resulting failure strains are shown in Fig. 10(a) for Docol 600DL and in Fig. 10 (b) for Docol 1400M, labelled by strain control, i.e., with the velocity gradient collected from the FE simulations. The corresponding failure predictions are represented by red triangles in the force-displacement curves in Fig. 3. While there are marked differences between the predicted localization strains and the failure strains obtained by the experimental-numerical method in Fig. 10, the displacement at failure in the tests in Fig. 3 is predicted with reasonable accuracy. The accuracy is particularly good for Docol 600DL, while for Docol 1400M the result is non-conservative for the NK tests. In plane-strain tension, the localization analysis gives somewhat conservative prediction for both Docol 600DL and Docol 1400M. With regards to the NK tests for Docol 1400M, ductile failure could take place before strain localization [3] and therefore the proposed approach would overestimate the ductility of the material. Another possible explanation could be that the low work-hardening of Docol 1400DL makes the NK tests more sensitive to small imperfections on the surface of the specimens. As the finite element models are built assuming a perfect surface geometry, the ductility would then be overestimated.

The through-thickness inclination of the critical band for the two different steel grades and the three different material tests are given in Table 3. At localization, the azimuth angle θ is equal to 90° for the UT and PST tests, while it is indeterminate for the NK test as the in-plane principal stresses are equal. It was concluded by Rudnicki and Rice [50] that localization under ordinary conditions takes place within a planar band with normal in the plane defined by the major and minor principal stress directions for isotropic materials. Both for the UT and PST tests, the X_2 axis coincides with the intermediate principal stress direction in the critical element towards localization. Note that after necking the stress state is not uniaxial in the critical location of the UT test specimen, see also Fig. 8. The polar angle ϕ is ~45° for all cases, i.e., the localization occurs in a planar band with normal lying in the X_1X_3 plane and making an angle of about 45° with the X_1 axis (RD).

While material tests usually produce non-proportional loadings locally, it is not unusual to average the stress state parameters, cf. Eqn. (16). By running localization analyses with a prescribed constant stress state outside the band, it is possible to evaluate the effect of having a proportional load path on the failure strain. This is carried out using the same approach as in Nahshon and Hutchinson [34]. The average stress triaxiality and Lode parameter listed in Table 2 are then applied outside the bands and the material is strained until loss of ellipticity occurs. To get the same accuracy as in the previous section the strain increments are controlled to be equal to 1×10^{-5}. Fig. 10 shows the results of averaging the stress state outside the band on the strain at localization (labelled stress control). While the stress-state averaging has minor influence for the PST tests and the NK tests, it has a strong impact on the predicted localization strain in the UT tests. This effect might be explained by the stress state evolution shown in Fig. 8. In the UT tests, the local stress state is drifting towards plane strain tension. By enforcing a constant stress state outside the band further away from $\mu = 0$, localization is delayed and the ductility is therefore increased. For the PST and NK tests, the averaged stress state is close to the actual one in the last stage before failure. As a result, the failure strain obtained under proportional loading is very similar to that obtained under the non-proportional load path.

Fig. 11 shows some details from the localization analyses performed for the Docol 600DL under strain control. Results from the critical bands and the material both outside and inside these bands are shown in the figure. Similar results were found for Docol 1400M. Fig. 11(a) illustrates the stress-strain behaviour (in terms of the von Mises equivalent stress), while Fig. 11(b) shows the evolution of the hydrostatic stress. The material inside the band has an initial work-hardening rate similar to the material outside due to the low value of the initial damage, but damage growth eventually lowers the work-hardening inside the band. Strain localization occurs when the work-hardening rate is negative for the UT and NK tests, while it is equal to zero for the PST test. The hydrostatic stress also shows different evolutions inside and outside the band. The band exhibits a larger pressure in the case of the UT and PST tests, while a lower pressure is observed for the NK test.

The evolutions of the equivalent plastic strain inside the critical band as a function of the Lode parameter and the stress triaxiality are shown in Fig. 11(c) and (d), respectively. The band follows the load path imposed by the outside material until the stress state drifts away and loss of ellipticity occurs. While the stress states inside the band at localization do not follow any specific trends in terms of stress triaxiality, the Lode parameter at localization is always close to zero (implying a generalized shear stress state) independently of the stress state outside the band. Since shear banding occurs more readily under generalized shear stress states, the band tries to reach this region of the stress space. This observation also supports the strong differences observed for the proportional and non-proportional loading of the UT test (cf. Fig. 10). In the strain-controlled analysis of the UT test, the stress state outside the band is already moving towards a generalized shear stress state, which promotes localization inside the band. Whereas in the stress-controlled loading, the Lode parameter is constant outside the band and consequently the band has to undergo more deformation to reach a generalized shear stress state. Thus, the apparent ductility of the material is larger when a proportional loading is applied.

Assuming that the localization analyses are able to represent the ductile failure mechanism, it is interesting to evaluate the shape of the failure locus of Docol 600DL. Fig. 12(a) shows the equivalent plastic strain obtained outside the band at localization under proportional loading and plane-stress conditions with stress triaxiality ranging from 0.45 to 0.66. The resulting failure locus shows the typical trends observed in ductile failure of metals with a plane-strain tension valley marked by a reduction of the ductility towards plane-strain tension and an increased ductility towards uniaxial and equi-biaxial tension, see e.g. [51]. A strong dissymmetry in terms of the Lode parameter is also present even if the constitutive model adopted for the material inside and outside the band has a symmetric dependency of this parameter. Similar observations were made by Dunand and Mohr [14] and Fourmeau et al. [52]. In terms of local stress states, Fig. 12(b) shows the evolution of the stress triaxiality and Lode parameter inside the band in red compared to the plane stress locus and stress states outside the band in black. As observed in Fig. 11(c) and (d), the stress state inside the band is always drifting away from the one imposed by the outside material towards generalized shear stress states. Strong deviations are also present in terms of stress triaxiality, and at localization the stress state is close to plane-strain tension, which is a generalized shear stress state.

Conclusions

An experimental programme was conducted on dual-phase and martensitic steel sheet materials comprising four material tests with stress states ranging from simple shear to equi-biaxial tension. The failure strain of the steel sheet materials was estimated using an experimental-numerical approach and the sensitivity of the ductility on the spatial discretization in the various tests was studied. It is found that the dual-phase steel displays a more ductile behaviour than the martensitic steel, and the strains are more localized in the test specimens made of the martensitic steel. Further, the estimated failure strain in the uniaxial tension and plane-strain tension tests is significantly influenced by the spatial discretization, which is in contrast to what was observed in the in-plane simple shear and equi-biaxial tension tests. The dependence of the estimated failure strain on spatial discretization, or length scale, is not related to high strain gradients alone. Also the shear specimens experience high gradients in the strain field, but only along the in-plane transverse direction and in this case the mesh dependence is minor. However, a strong dependence of the spatial discretization seems to be related to the presence of necking instabilities or high multi-axial strain gradients which occur in the uniaxial tension and plane-strain tension tests. The different mesh sensitivity of the estimated failure strain in the various tests implies that a simple scaling of the failure locus, e.g. according to a version of Barba's law, may lead to significant inaccuracies in simulation of fracture initiation. Applying an imperfection band approach in combination with the Gurson model, localization analysis was used to estimate the strain at localization in the uniaxial tension, plane-strain tension and Nakajima tests. The obtained results were promising and indicate that localization analysis may be used to establish a conservative failure criterion for ductile materials, provided strain localization occurs prior to ductile fracture. The analyses show that the stress state inside the band tends to move towards generalized shear before onset of localization.

Acknowledgement

The financial support from the Eurostar Programme with project number E! 6951 GEPEU is highly acknowledged.

References

[1] McClintock, F. A. (1968). Criterion for ductile fracture by growth of holes. Journal of Applied Mechanics **35**: 363-371.

[2] Rice, J. R. and Tracey, D. M. (1969). On the ductile enlargement of voids in triaxial stress fields. Journal of the Mechanics and Physics of Solids **17**: 201-217.

[3] Tekoğlu, C., Hutchinson, J. W. and Pardoen, T. (2015). On localization and void coalescence as a precursor to ductile fracture. Philosophical Transactions of the Royal Society of London A: Mathematical, Physical and Engineering Sciences **373**(2038).

[4] Bridgman, P. W. (1952). Studies in large plastic flow and fracture: with special emphasis on the effects of hydrostatic pressure. Cambridge, Mass., Harvard Univ. Press.

[5] Hopperstad, O. S., Børvik, T., Langseth, M., Labibes, K. and Albertini, C. (2003). On the influence of stress triaxiality and strain rate on the behaviour of a structural steel. Part I. Experiments. European Journal of Mechanics - A/Solids **22**(1): 1-13.

[6] Hancock, J. W. and Mackenzie, A. C. (1976). On the mechanisms of ductile failure in high-strength steels subjected to multi-axial stress-states. Journal of the Mechanics and Physics of Solids **24**(2-3): 147-169.

[7] Johnson, G. R. and Cook, W. H. (1985). Fracture characteristics of three metals subjected to various strains, strain rates, temperatures and pressures. Engineering Fracture Mechanics **21**(1): 31-48.

[8] Bao, Y. and Wierzbicki, T. (2004). On fracture locus in the equivalent strain and stress triaxiality space. International Journal of Mechanical Sciences **46**: 81-98.

[9] Barsoum, I. and Faleskog, J. (2007). Rupture mechanisms in combined tension and shear—Experiments. International Journal of Solids and Structures **44**(6): 1768-1786.

[10] Mohr, D. and Ebnoether, F. (2009). Plasticity and fracture of martensitic boron steel under plane stress conditions. International Journal of Solids and Structures **46**(20): 3535-3547.

[11] Gruben, G., Vysochinskiy, D., Coudert, T., Reyes, A. and Lademo, O.-G. (2013). Determination of ductile fracture parameters of a dual-phase steel by optical measurements. Strain **49**(3): 221-232.

[12] Gao, X. and Kim, J. (2006). Modeling of ductile fracture : Significance of void coalescence. International Journal of Solids and Structures **43**: 17.

[13] Barsoum, I. and Faleskog, J. (2011). Micromechanical analysis on the influence of the Lode parameter on void growth and coalescence. International Journal of Solids and Structures **48**(6): 925-938.

[14] Dunand, M. and Mohr, D. (2014). Effect of Lode parameter on plastic flow localization after proportional loading at low stress triaxialities. Journal of the Mechanics and Physics of Solids **66**: 133-153.

[15] Lode, W. (1926). Versuche über den Einfluß der mittleren Hauptspannung auf das Fließen der Metalle Eisen, Kupfer und Nickel. Zeitschrift für Physik A Hadrons and Nuclei **36**: 913-939.

[16] Gruben, G., Hopperstad, O. S. and Børvik, T. (2012). Evaluation of uncoupled ductile fracture criteria for the dual-phase steel Docol 600DL. International Journal of Mechanical Sciences **62**: 133-146.

[17] Davis, J. R. (2004). Tensile Testing, ASM International.

[18] Yamada, Y. (2006). Bulbous Buffer Bow: A Measure to Reduce Oil Spill in Tanker Collisions. Department of Mechanical Engineering. Lyngby, Denmark, Technical University of Denmark. PhD thesis.

[19] Ehlers, S., Broekhuijsen, J., Alsos, H. S., Biehl, F. and Tabri, K. (2008). Simulating the collision response of ship side structures: A failure criteria benchmark study. International Shipbuilding Progress **55**(1-2): 127-144.
[20] Hogström, P. (2012). RoPax Ship Collision – a Methodology for Survivability Analysis Department of Shipping and Marine Technology. Gothenburg, Sweden, Chalmers University of Technology. PhD thesis.
[21] Wilkins, M. L., Streit, R. D. and Reaugh, J. E. (1980). Cumulative-strain-damage model of ductile fracture: simulation and prediction of engineering fracture tests. Lawrence Livermore National Laboratory. Report.
[22] Hancock, J. W. and Brown, D. K. (1983). On the role of strain and stress state in ductile failure. Journal of the Mechanics and Physics of Solids **31**(1): 1-24.
[23] Børvik, T., Hopperstad, O. S. and Berstad, T. (2003). On the influence of stress triaxiality and strain rate on the behaviour of a structural steel. Part II. Numerical study. European Journal of Mechanics - A/Solids **22**(1): 15-32.
[24] Gruben, G., Fagerholt, E., Hopperstad, O. S. and Børvik, T. (2011). Fracture characteristics of a cold-rolled dual-phase steel European Journal of Mechanics - A/Solids **30**: 204-218.
[25] Björklund, O., Govik, A. and Nilsson, L. (2014). Prediction of fracture in a dual-phase steel subjected to non-linear straining. Journal of Materials Processing Technology **214**(11): 2748-2758.
[26] Björklund, O. and Nilsson, L. (2014). Failure characteristics of a dual-phase steel sheet. Journal of Materials Processing Technology **214**(6): 1190-1204.
[27] Fagerholt, E., Borvik, T. and Hopperstad, O. S. (2013). Measuring discontinuous displacement fields in cracked specimens using digital image correlation with mesh adaptation and crack-path optimization. Optics and Lasers in Engineering **51**(3): 299-310.
[28] Dunand, M. and Mohr, D. (2010). Hybrid experimental-numerical analysis of basic ductile fracture experiments for sheet metals. International Journal of Solids and Structures **47**(9): 1130-1143.
[29] Marciniak, Z. and Kuczyński, K. (1967). Limit strains in the processes of stretch-forming sheet metal. International Journal of Mechanical Sciences **9**(9): 609-620.
[30] Rice, J. R. (1977). The localization of plastic deformation. Delft, North-Holland Publishing.
[31] Yamamoto, H. (1978). Conditions for shear localization in the ductile fracture of void-containing materials. International Journal of Fracture **14**(4): 347-365.
[32] Saje, M., Pan, J. and Needleman, A. (1982). Void nucleation effects on shear localization in porous plastic solids. International Journal of Fracture **19**(3): 163-182.
[33] Pan, J., Saje, M. and Needleman, A. (1983). Localization of deformation in rate sensitive porous plastic solids. International Journal of Fracture **21**(4): 261-278.
[34] Nahshon, K. and Hutchinson, J. W. (2008). Modification of the Gurson Model for shear failure. European Journal of Mechanics - A/Solids **27**(1): 1-17.
[35] Haddag, B., Abed-Meraim, F. and Balan, T. (2009). Strain localization analysis using a large deformation anisotropic elastic–plastic model coupled with damage. International Journal of Plasticity **25**(10): 1970-1996.
[36] Gruben, G., Langseth, M., Fagerholt, E. and Hopperstad, O. S. (2016). Low-velocity impact on high-strength steel sheets: An experimental and numerical study. International Journal of Impact Engineering **88**: 153-171.
[37] Nakajima, K., Kikuma, T. and Hasuka, K. (1968). Study on the formability of steel sheets. Report. 8517-8530.
[38] IMPETUS. "www.impetus-afea.com." Retrieved 13.06, 2016.

[39] Hershey, A. V. (1954). The Plasticity of an Isotropic Aggregate of Anisotropic Face-Centered Cubic Crystals. Journal Applied Mechanics **76**: 241-249.

[40] Gurson, A. L. (1977). Continuum theory of ductile rupture by void nucleation and growth, 1. Yield criteria and flow rules for porous ductile media. Journal of Engineering Materials and Technology-Transactions of the ASME 99(1): 2-15.

[41] Tvergaard, V. (1981). Influence of voids on shear band instabilities under plane strain conditions. International Journal of Fracture **17**(4): 389-407.

[42] Steglich, D., Wafai, H. and Besson, J. (2010). Interaction between anisotropic plastic deformation and damage evolution in Al 2198 sheet metal. Engineering Fracture Mechanics **77**(17): 3501-3518.

[43] Chu, C. C. and Needleman, A. (1980). Void Nucleation Effects in Biaxially Stretched Sheets. Journal of Engineering Materials and Technology **102**(3): 249-256.

[44] Nielsen, K. L. and Tvergaard, V. (2009). Effect of a shear modified Gurson model on damage development in a FSW tensile specimen. International Journal of Solids and Structures **46**(3–4): 587-601.

[45] Zhou, J., Gao, X., Sobotka, J. C., Webler, B. A. and Cockeram, B. V. (2014). On the extension of the Gurson-type porous plasticity models for prediction of ductile fracture under shear-dominated conditions. International Journal of Solids and Structures **51**(18): 3273-3291.

[46] Nielsen, K. L. and Tvergaard, V. (2010). Ductile shear failure or plug failure of spot welds modelled by modified Gurson model. Engineering Fracture Mechanics **77**(7): 1031-1047.

[47] Balan, T., Lemoine, X., Maire, E. and Habraken, A.-M. (2015). Implementation of a damage evolution law for dual-phase steels in Gurson-type models. Materials & Design **88**: 1213-1222.

[48] Landron, C., Maire, E., Bouaziz, O., Adrien, J., Lecarme, L. and Bareggi, A. (2011). Validation of void growth models using X-ray microtomography characterization of damage in dual phase steels. Acta Materialia **59**(20): 7564-7573.

[49] Besson, J., Steglich, D. and Brocks, W. (2001). Modeling of crack growth in round bars and plane strain specimens. International Journal of Solids and Structures **38**(46–47): 8259-8284.

[50] Rudnicki, J. W. and Rice, J. R. (1975). Conditions for the localization of deformation in pressure-sensitive dilatant materials. Journal of the Mechanics and Physics of Solids **23**(6): 371-394.

[51] Gu, G. and Mohr, D. (2015). Anisotropic Hosford–Coulomb fracture initiation model: Theory and application. Engineering Fracture Mechanics **147**: 480-497.

[52] Fourmeau, M., Marioara, C. D., Børvik, T., Benallal, A. and Hopperstad, O. S. (2015). A study of the influence of precipitate-free zones on the strain localization and failure of the aluminium alloy AA7075-T651. Philosophical Magazine **95**(28-30): 3278-3304.

Tables and figures

Table 1 Constitutive model parameters for the two materials.

Material	σ_0 [MPa]	Q_1 [MPa]	C_1	Q_2 [MPa]	C_2	Q_3 [MPa]	C_3	$\dot{p}_0$ [s^{-1}]	c	m
600DL	317	201	38.4	348	5.00	6000	$1.00 \cdot 10^{-2}$	$3.0 \cdot 10^{-3}$	$9.0 \cdot 10^{-3}$	6.0
1400M	1200	254	774	97.0	135	200	6.00	$1.0 \cdot 10^{-1}$	$4.0 \cdot 10^{-3}$	6.0

Table 2 Failure strain, p_f, average stress triaxiality, σ^*_{avg}, and average Lode parameter, μ_{avg}, obtained with the experimental-numerical approach.

Material	Variable	p-order	UT	PST	ISS	NK
Docol 600DL	p_f	1-linear	0.772	0.645	0.982	0.994
		2-quadratic	0.853	0.733	0.989	0.997
		3-cubic	0.995	0.773	0.996	0.999
	σ^*_{avg}	1-linear	0.403	0.574	0.025	0.661
		2-quadratic	0.426	0.600	0.052	0.665
		3-cubic	0.468	0.610	0.042	0.665
	μ_{avg}	1-linear	-0.814	-0.186	-0.061	0.938
		2-quadratic	-0.765	-0.155	-0.036	0.938
		3-cubic	-0.683	-0.144	-0.110	0.937
Docol 1400M	p_f	1-linear	0.619	0.266	0.750	0.594
		2-quadratic	0.809	0.391	0.792	0.592
		3-cubic	0.854	0.427	0.763	0.592
	σ^*_{avg}	1-linear	0.473	0.597	0.094	0.664
		2-quadratic	0.523	0.635	0.118	0.663
		3-cubic	0.516	0.647	0.129	0.662
	μ_{avg}	1-linear	-0.686	-0.084	-0.232	0.998
		2-quadratic	-0.622	-0.051	-0.291	0.998
		3-cubic	-0.593	-0.046	-0.310	0.998

708 Table 3 Through-thickness inclination (or polar angle ϕ) of planer band at localization.

Specimen	Docol 600DL	Docol 1400M
UT	44.00°	45.04°
PST	44.31°	44.56°
NK	43.85°	44.35°

709

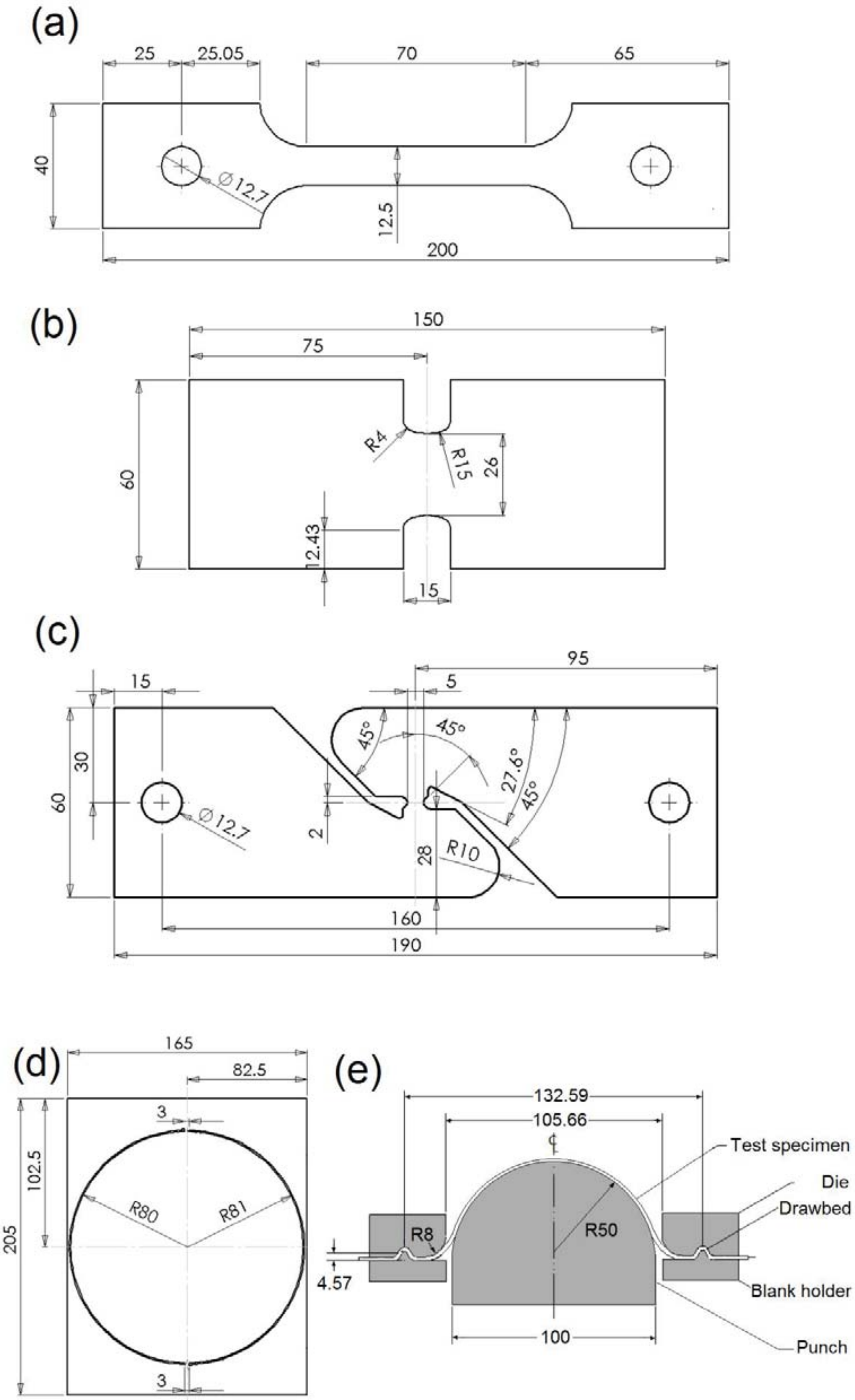

Fig. 1 Nominal specimen geometry: (a) uniaxial tension test, (b) plane-strain tension test, (c) in-plane simple shear test and (d) equi-biaxial Nakajima test. Details of the Nakajima set-up are shown in (e).

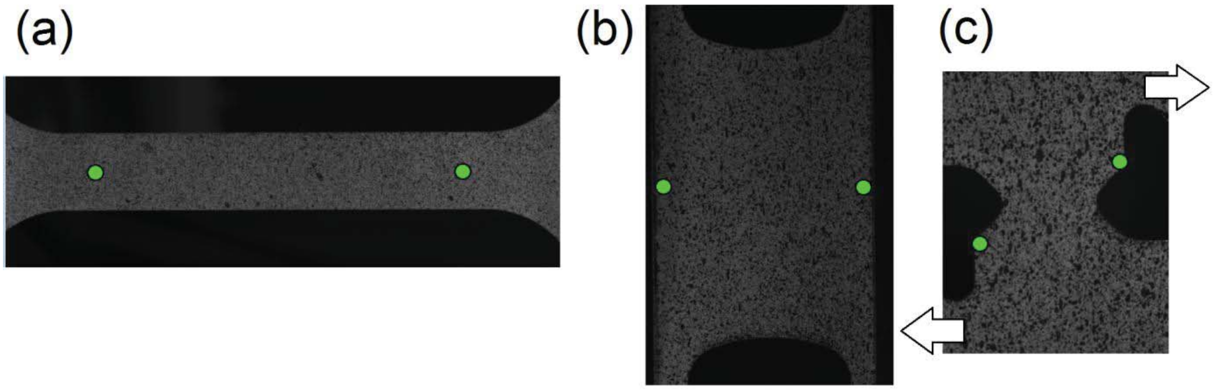

Fig. 2 Position of virtual extensometer in (a) uniaxial tension test, (b) plane-strain tension test and (c) in-plane simple shear test.

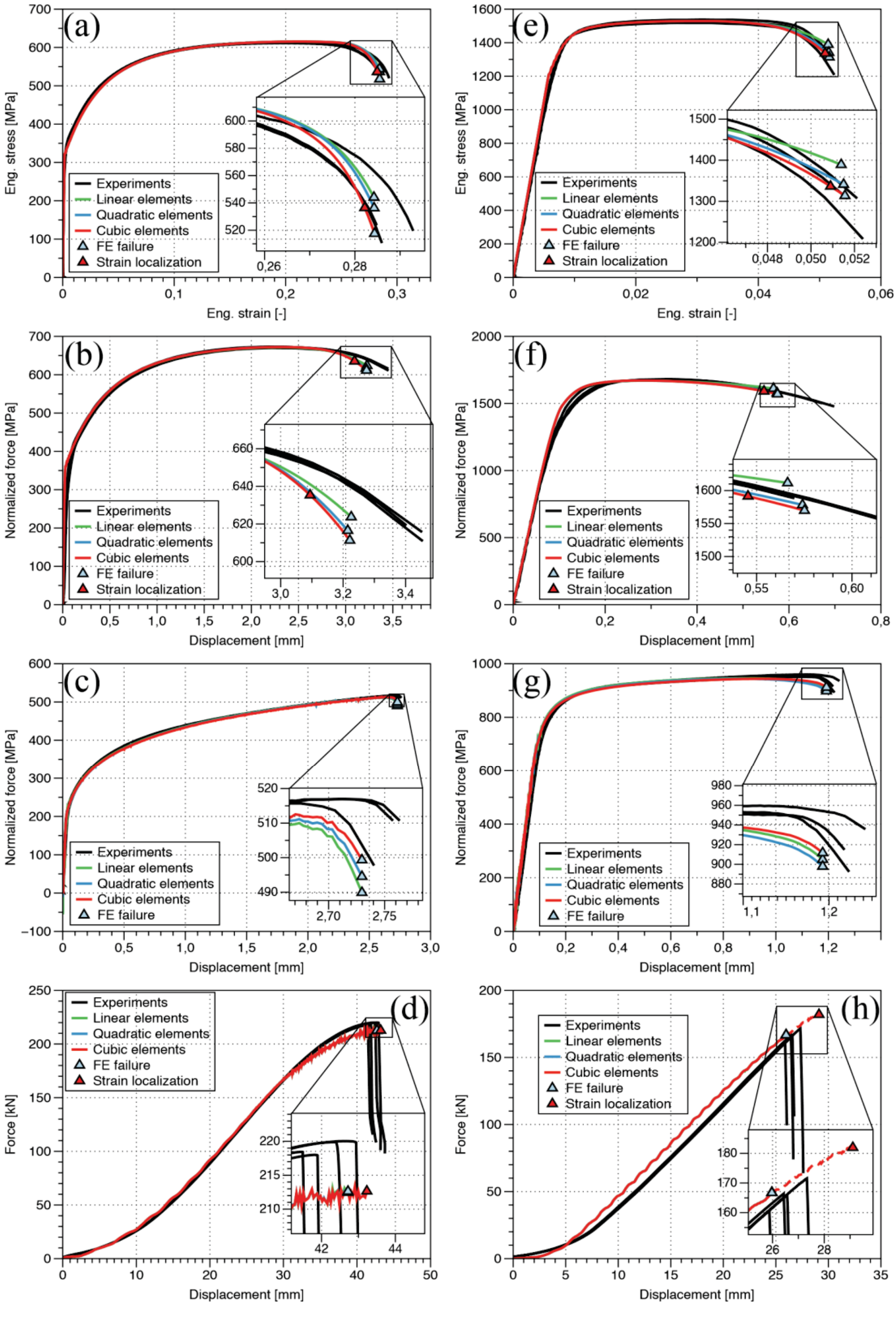

Fig. 3 Global response curves from experiments and FE simulations of (a)-(d) Docol 600DL and (e)-(h) Docol 1400M: (a),(e) engineering stress-strain curves in uniaxial tension; (b),(f) normalized force versus displacement curves in plane-strain tension; (c),(g) normalized force versus displacement curves in in-plane simple shear; (d),(h) force-displacement curves from Nakajima tests in equi-biaxial tension.

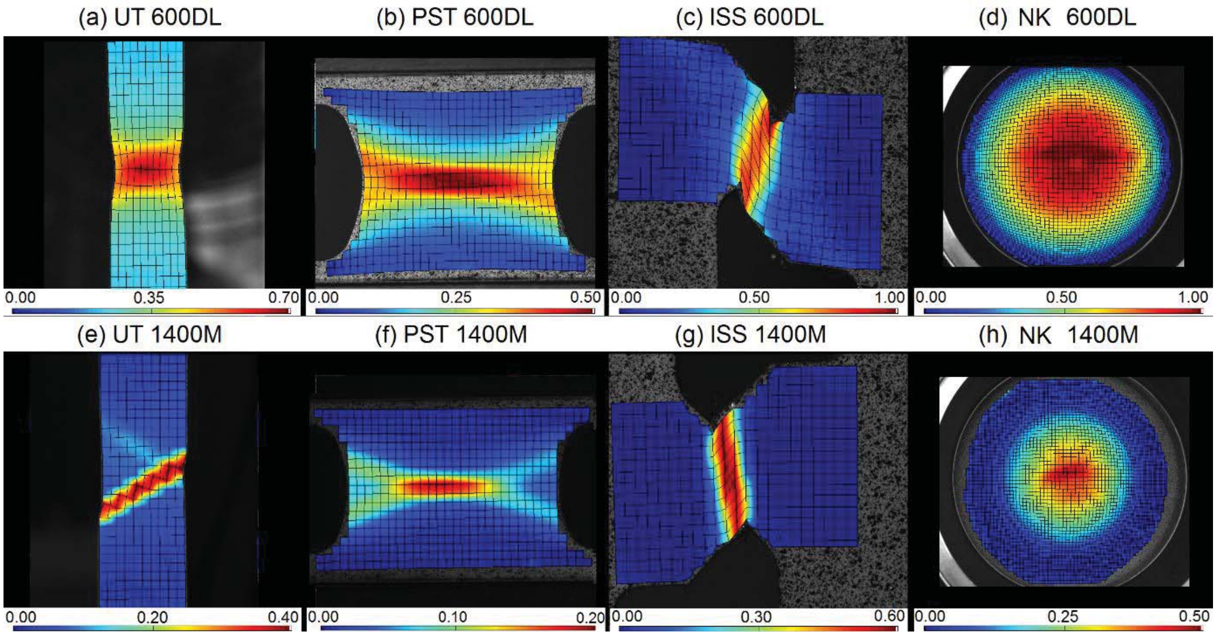

Fig. 4 Strain magnitude field from the last image before onset of fracture in selected duplicates of the experimental tests.

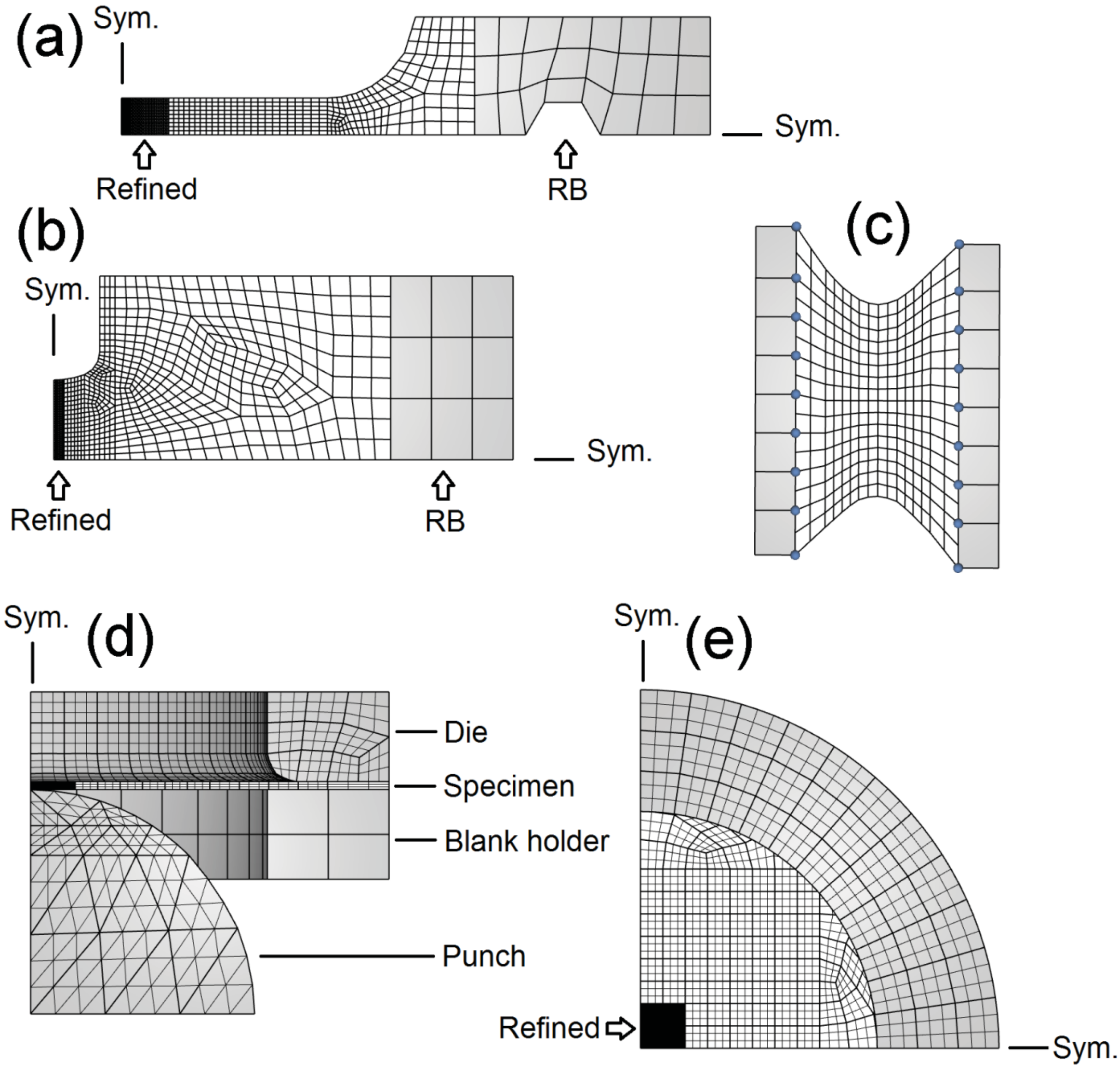

Fig. 5 Finite element meshes of (a) uniaxial tension test, (b) plane-strain tension test, (c) in-plane simple shear test and (d-e) Nakajima test in equi-biaxial tension. In-plane symmetry is marked for the uniaxial tension, plane-strain tension and Nakajima specimens.

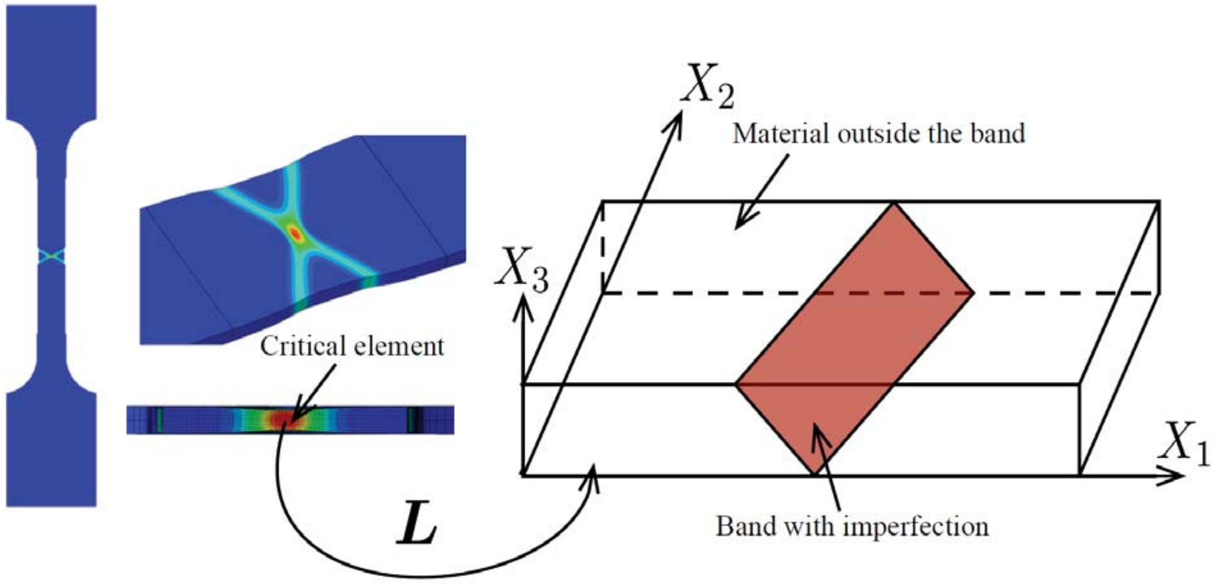

Fig. 6 Illustration of localization analysis: position of the critical element in simulation of the uniaxial tensile test (left); orientation of imperfection band with respect to the rolling direction (X_1), in-plane transverse direction (X_2), and normal direction (X_3) of the sheet.

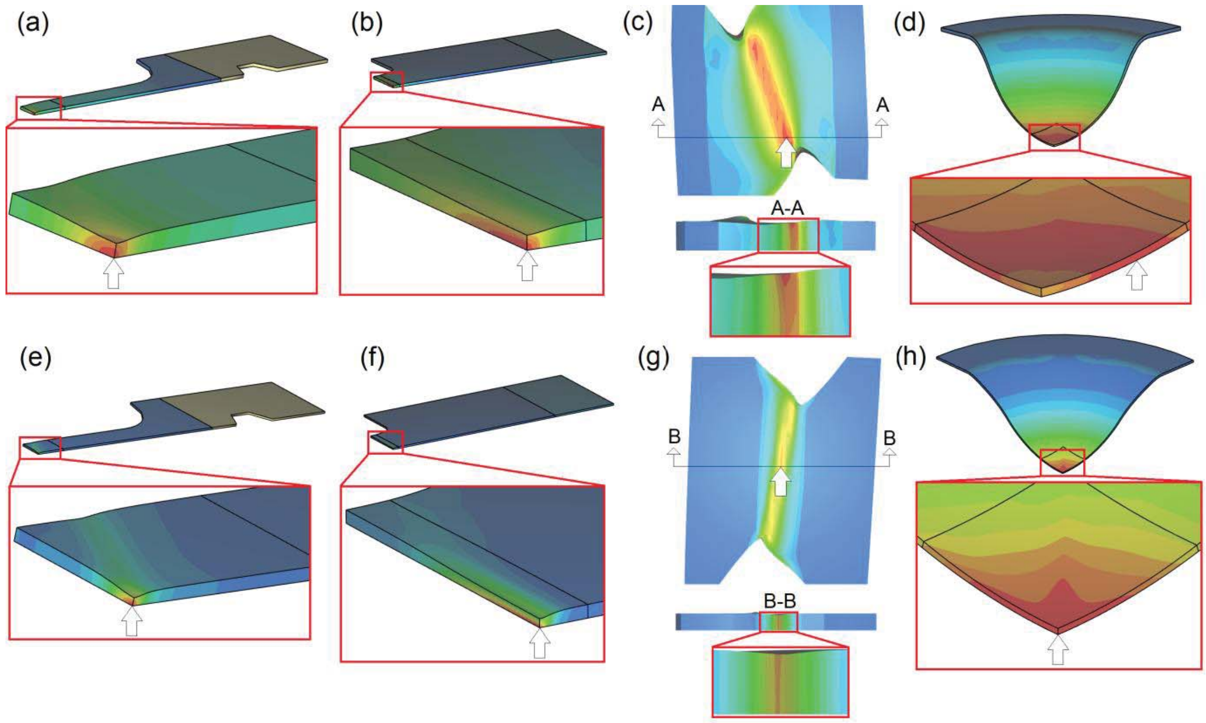

Fig. 7 Equivalent plastic strain fields before onset of fracture in cubic element simulations of (a-d) Docol 600DL and (e-h) Docol 1400M: (a),(e) uniaxial tension test; (b),(f) plane-strain tension test; (c),(g) in-plane simple shear test; (d),(h) equi-biaxial Nakajima test. The positions of the critical elements, i.e., the positions in the FE models corresponding to the experimental point of fracture initiation, are marked by arrows.

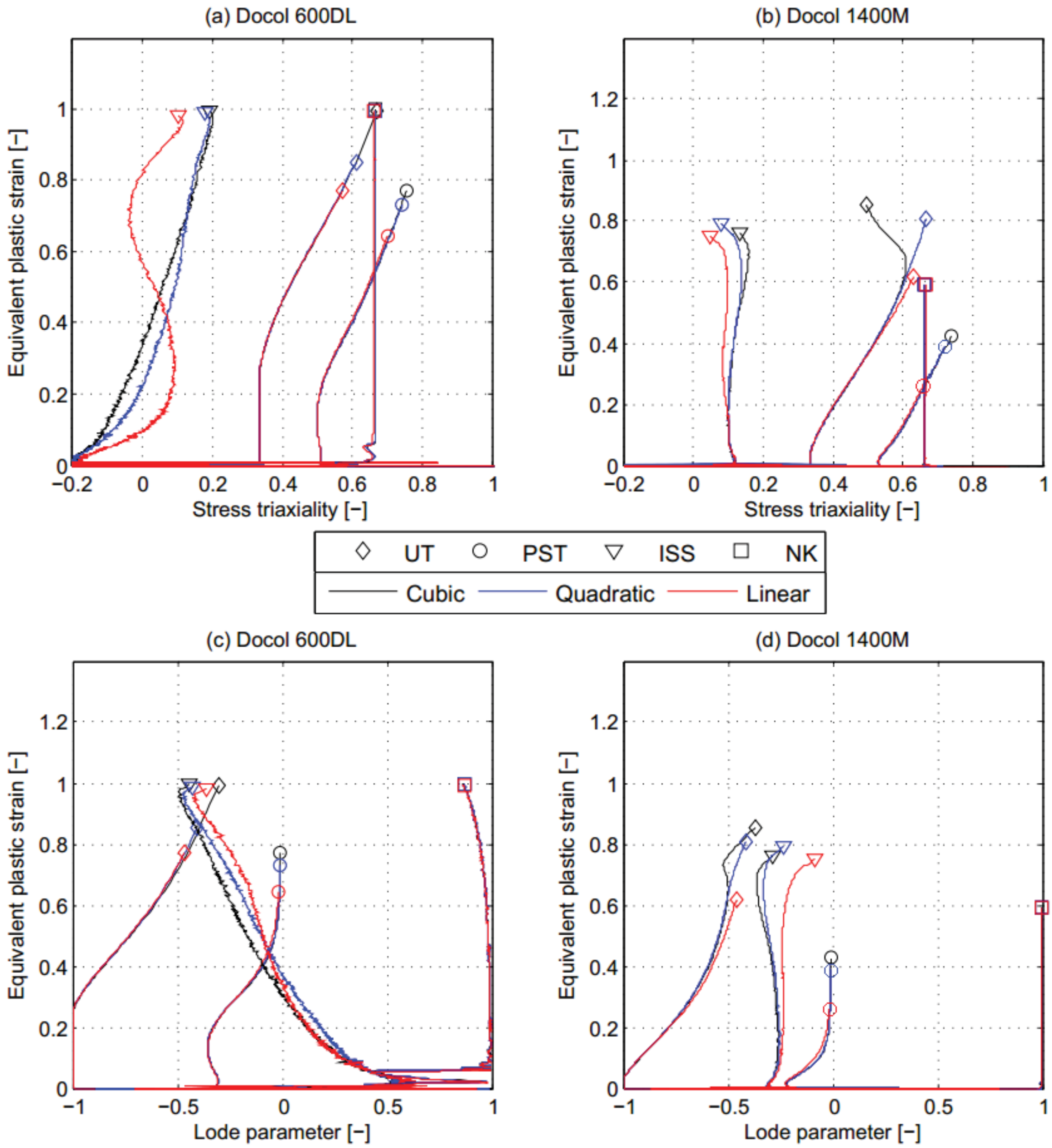

Fig. 8 Stress and strain histories collected from critical elements in simulations of the material tests: (a),(b) equivalent plastic strain versus stress triaxiality; (c),(d) equivalent plastic strain versus Lode parameter. The curves are generated from simulations with linear, quadratic and cubic shape functions.

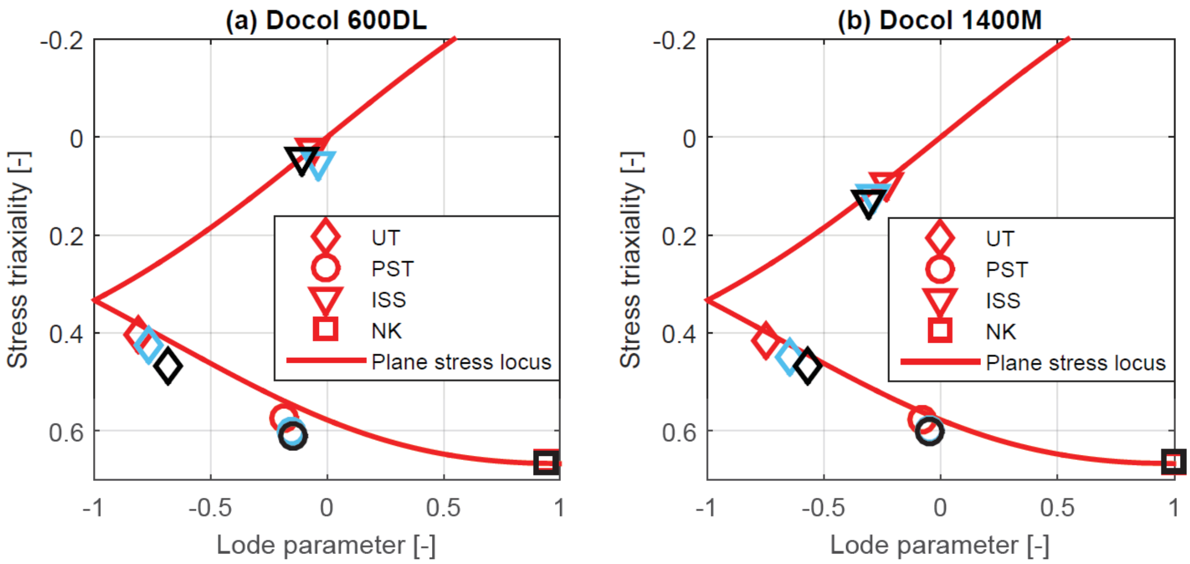

Fig. 9 Simulated average values of stress triaxiality and Lode parameter in tests compared with plane stress locus: (a) Docol 600DL and (b) Docol 1400M. Red, blue and black markers present results from simulations with linear, quadratic and cubic elements, respectively.

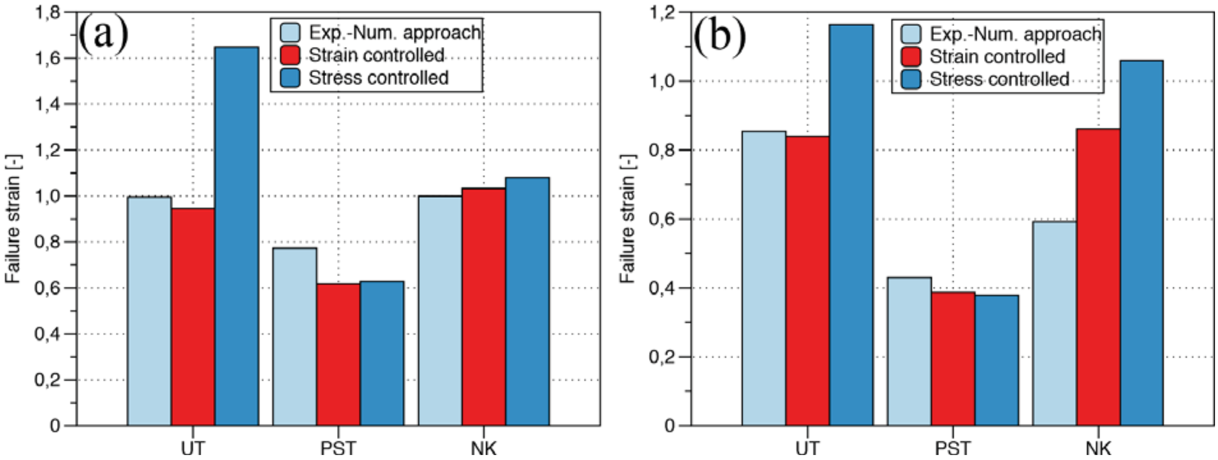

Fig. 10 Failure strain from hybrid experimental-numerical approach and failure strain estimated with the localization analysis: (a) Docol 600DL and (b) Docol 1400M. Strain control means that the localization analysis was performed using the strain history from the FE simulation, thus giving non-proportional loading, while stress control means that the average values of the stress triaxiality and Lode parameter were imposed to ensure proportional loading.

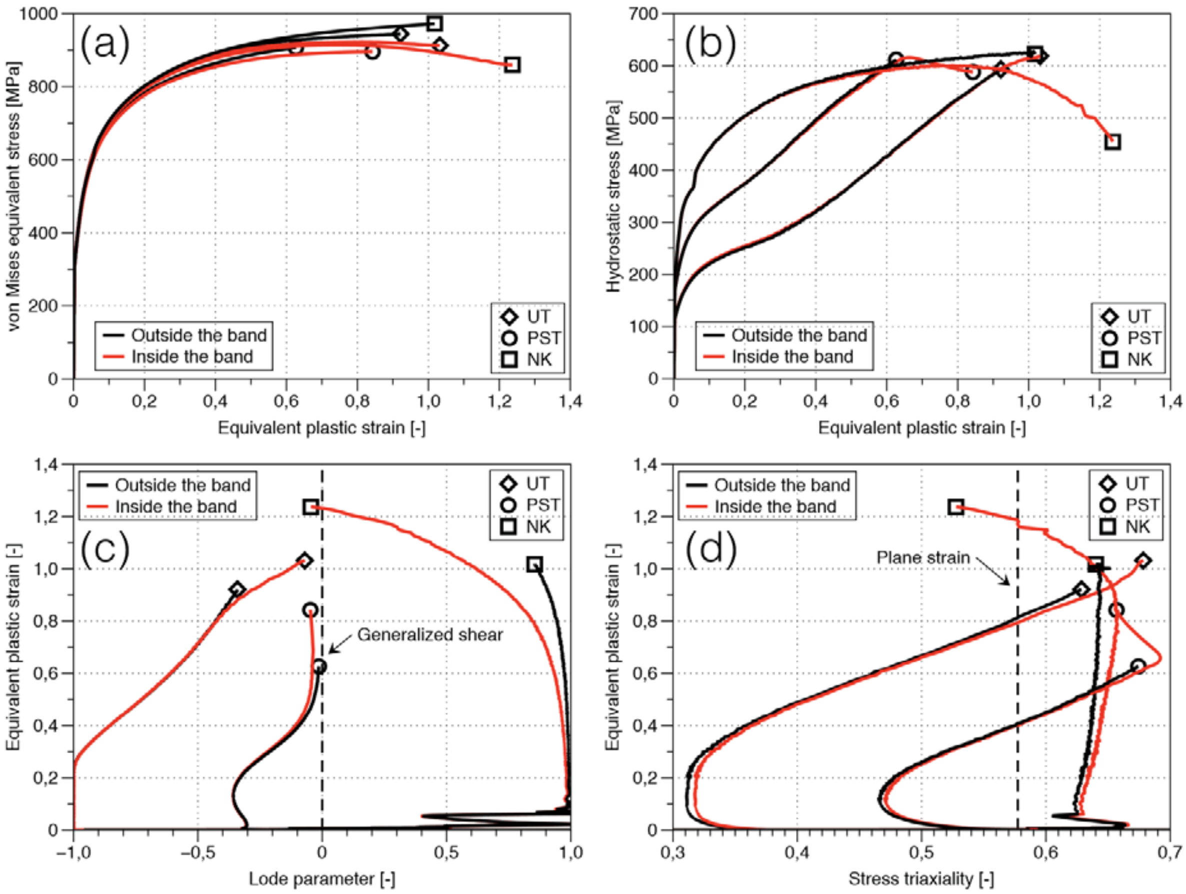

Fig. 11 Details from the band analysis of the UT, PST and NK simulations for Docol 600DL: (a) von Mises equivalent stress vs. equivalent plastic strain, (b) hydrostatic stress vs. equivalent plastic strain, (c) equivalent plastic strain vs. Lode parameter and (d) equivalent plastic strain vs. stress triaxiality. All quantities are presented for the material outside and inside the critical band.

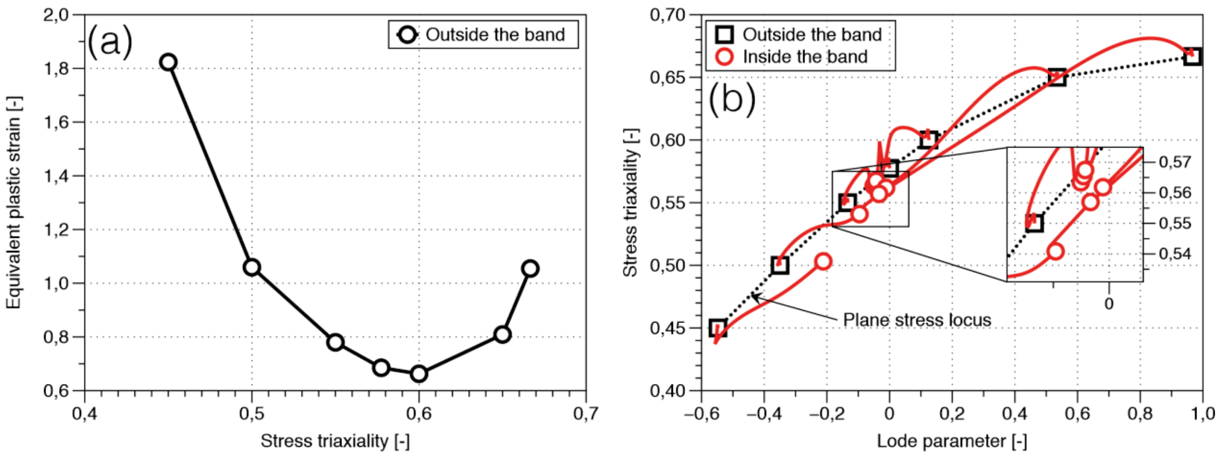

Fig. 12 (a) Plane-stress fracture locus for Docol 600DL based on quantities outside the band, and (b) stress triaxiality vs. Lode parameter inside and outside the critical band.